Electronic Supplementary Material (ESI) for Journal of Materials Chemistry A.
This journal is © The Royal Society of Chemistry 2023

Electronic Supplementary Material

Understanding the role of Zn vacancy induced by sulfhydryl coordination for photocatalytic CO_2 reduction on $ZnIn_2S_4$

Yu Nie [a], Tingting Bo [c], Wei Zhou *[c], Huilin Hu [d], Xiang Huang [e], Huaiyuan Wang *[b], Xin Tan [a,e], Lequan Liu [d], Jinhua Ye [f], Tao Yu *[b]

[a] School of Environmental Science and Engineering, Tianjin University, No. 135 Yaguan Road, Jinnan District, Tianjin, 300350, China
[b] School of Chemical Engineering and Technology, Tianjin University, No. 135 Yaguan Road, Jinnan District, Tianjin, 300350, China
[c] School of Science, Tianjin University, No. 135 Yaguan Road, Jinnan District, Tianjin, 300350, China
[d] TJU-NIMS International Collaboration Laboratory, Tianjin University, No. 92 Weijin Road, Nankai District, Tianjin, 300072, China
[e] School of Science, Tibet University, No. 36 Jiangsu Road, Lhasa, 850000, China
[f] International Center for Materials Nanoarchitectonics (WPI-MANA) National Institute for Materials Science (NIMS), 1-1 Namiki, Tsukuba 305-0047, Japan

Text S1. Time-resolved transient photoluminescence lifetime

Time-resolved transient photoluminescence was exploited to appraise the carrier lifetime of catalyst, and fitted using a biexponential function. Their lifetimes (τ_i), average lifetimes (Ave.τ) and amplitudes (A_i) were calculated according to **Equations (1), (2)** and displayed in **Table. S5**.

Eq.(1)

$$I(t) = A_1 \exp\left(-\frac{t}{\tau_1}\right) + A_2 \exp\left(-\frac{t}{\tau_2}\right)$$

Eq.(2)

$$Ave.\tau = \frac{A_1\tau_1^2 + A_2\tau_2^2}{A_1\tau_1 + A_2\tau_2}$$

Text S2. Photoelectrochemical measurements

The photoelectrochemical properties were investigated in a three-electrode cell by using CHI660E workstation (Chenhua, Shanghai). The as-synthesized samples coated on pretreated indium–tin oxide (ITO) conductor glass, a Pt wire, an Ag/AgCl electrode and Na_2SO_4 (0.1 M) aqueous solution were used as the working electrode, the counter-electrode, the reference electrode, and the electrolyte, respectively. A 300 W Xenon lamp equipped with a 420 nm cutoff filter was utilized as a light source. The photocurrent with ON/OFF cycles was measured at an applied potential of 0.5 V *versus* Ag/AgCl, sample interval (s) = 0.1, run time (sec) = 600, quiet time (sec) = 0, sensitivity (A/V) = 10^{-5}. The electrochemical impedance spectroscopy (EIS) was taken in the frequency range of 10^4 −0.01 Hz at the open circuit potential. Linear sweep voltammetry (LSV) was carried out in an CO_2-saturated 0.5 M $KHCO_3$ solution (pH=7.3) with a scan rate of 10 mV s^{-1}. To prepare the working electrode, 10 mg samples were first dispersed into ethanol (450 µL) and Nafion (50 µL) mixtures using soft ultrasonic stirring to obtain a uniform suspension. The solution containing the samples (100 µL) was dropped onto the pretreated ITO conductor glass substrate (ca. 1×1 cm^2), which were then dried in an oven at 60 ºC overnight.

Text S3. Computational details

In this work, all calculations were calculated by the first principles based on the Vienna Ab initio Simulation Package (VASP).[1, 2] The generalized gradient approximation (GGA) functional of Perdew, Burke and Ernzerhof is used and a vacuum thickness more than 15 Å is adopt to separate it from its periodic model.[3] The plane wave cutoff energy is set as 400 eV and the van der Waals (vdW) interactions are included by using the PBE-D2 functional.[4] Furthermore, the convergence criterion of total energy and residual force are 10^{-5} eV and 0.01 eV/Å, respectively. Here, we use $ZnIn_2S_4$ surface system. For the vacancy system, it is constructed by removing a surface Zn atom from the pure phase surface system. The surface model of $ZnIn_2S_4$(102) with 168 atoms and $ZnIn_2S_4$(001) with 28 atoms were used for CO_2 reduction and HER respectively.

Here, we analyze the effect of vacancy on the charge distribution of the surface system by Bader Charge and use pure $ZnIn_2S_4$ charge distribution for comparison. According to Bader Charge analysis, we found that the vacancy had a great influence on the charge of nearby S atoms, while the influence on other atoms was weak and can be ignored. We marked the S atoms with charge changes as S1, S2, S3 and S4, as shown in Figure 4.

In order to indicate HER performance of the main competitive reaction for CO_2 reduction in $ZnIn_2S_4$ system, the Gibbs free energy of HER path was calculated based on the computational hydrogen electrode (CHE) proposed by Nørskov et al.[5, 6] According to this method, the Gibbs free energy of the proton and electron pair ($H^+ + e^-$) is equal to half of the free energy of gaseous hydrogen (H_2) at standard reaction conditions. Moreover, the change Gibbs free energy (ΔG) of each species can be obtained from the following **Equation S3**.

Eq.(3)

$$\Delta G = \Delta E_{DFT} + \Delta E_{ZPE} - \Delta TS$$

where ΔE_{DFT} is the electronic energy calculated from DFT calculations, ΔE_{ZPE} is the zero-point energy the adsorbed species and ΔS is the entropy contribution at room temperature, respectively. In addition, the performance of CO_2 reduction was estimated by adsorption energy.

Table S1. Pore structure parameters of L-ZIS, $L_{0.75}T_{0.25}$-ZIS, $L_{0.5}T_{0.5}$-ZIS, $L_{0.25}T_{0.75}$-ZIS and T-ZIS

Materials	**BET ($m^2\ g^{-1}$)**	**Pore Volume ($cm^3\ g^{-1}$)**	**Pore Size (nm)**
L-ZIS	16.65	0.14	3.931
$L_{0.75}T_{0.25}$-ZIS	63.85	0.41	3.943
$L_{0.5}T_{0.5}$-ZIS	67.79	0.42	3.935
$L_{0.25}T_{0.75}$-ZIS	85.03	0.57	3.941
T-ZIS	66.74	0.31	3.937

The BET results of L-ZIS, $L_{0.75}T_{0.25}$-ZIS, $L_{0.5}T_{0.5}$-ZIS, $L_{0.25}T_{0.75}$-ZIS and T-ZIS were determined to 16.65, 63.85, 67.79, 85.03 and 66.74 $m^2\ g^{-1}$, respectively. $L_{0.25}T_{0.75}$-ZIS had the highest specific surface area so that it expressed best adsorption performance of CO_2 (Figure 6a). It was found that all samples were all mesoporous materials with 3.9 nm pore size.

Table S2. Elemental compositions of L-ZIS, $L_{0.75}T_{0.25}$-ZIS, $L_{0.5}T_{0.5}$-ZIS, $L_{0.25}T_{0.75}$-ZIS and T-ZIS determined by XPS analysis and ICP-OES

Photocatalysts	Zn		In		S	Total	
	XPS (%)	ICP-OES (ppm)	XPS (%)	ICP-OES (ppm)	XPS (%)	XPS normalization	ICP normalization
L-ZIS	8.12	3.006	29.95	13.93	60.14	$Zn_{0.54}In_{1.99}S_4$	$Zn_{0.76}In_2$
$L_{0.75}T_{0.25}$-ZIS	8.98	3.746	30.64	15.86	58.4	$Zn_{0.62}In_{2.1}S_4$	$Zn_{0.83}In_2$
$L_{0.5}T_{0.5}$-ZIS	10.57	2.907	29.93	11.1	57.17	$Zn_{0.74}In_{2.1}S_4$	$Zn_{0.92}In_2$
$L_{0.25}T_{0.75}$-ZIS	12.45	3.698	28.27	12.73	56.54	$Zn_{0.88}In_2S_4$	$Zn_{1.02}In_2$
T-ZIS	13.88	3.793	27.54	12.74	55.54	$ZnIn_{1.98}S_4$	$Zn_{1.05}In_2$

With increased of L-Cys, V_{Zn} concentrations were enhanced while mole of In:S was maintain 0.5 as NMR and FT-IR (Fig. 1b-d) designed.

Table S3. CO_2 reduction performance under various conditions

	Condition	CO generation (mmol g^{-1} h^{-1})	H_2 generation (mmol g^{-1} h^{-1})
1	no catalyst	0	0
2	no light	0	0
3	N_2 replace CO_2	0	0
4	no TEOA	0.23	0
5	no $Co(bpy)_3^{2+}$	0.06	0.09
6	$L_{0.25}T_{0.75}$-ZIS	5.63	0.24

In the absence of catalyst, light or CO_2, no product generated. When TEOA removed from reaction system, the CO yield was only 0.23 mmol g^{-1} h^{-1}. If change removed $Co(bpy)_3^{2+}$, CO production rate was just 0.06 mmol g^{-1} h^{-1}.

Table S4. Comparisons of reaction systems for CO_2 photoreduction of $ZnIn_2S_4$ catalysts

sacrificial agent	solvent	photosensitizer	Photocatalyst	light	product	selectivity（%）	yield（umol g^{-1} h^{-1}）	AQY	reference
			$ZnS@ZnIn_2S_4$	AM 1.5G	CO	84.3	87.43	2.43(420 nm)	[7]
			$ZnIn_2S_4/KCa_2Nb_3O_{10}$	300W Xe lamp	CO	86	4.69		[8]
			$ZnIn_2S_4/TiO_2$ nanobelts	300 W Xe lamp	CH_4	85.1	1.135		[9]
			$CuS@ZnIn_2S_4$	300 W Xe lamp	CH_4	43.6	94.5		[10]
			$ZnIn_2S_4/BiVO_4$	300W Xe lamp	CO	93.7	4.75		[11]
	No extras		$ZnIn_2S_4$	AM 1.5G	CO		33.2	0.23(400 nm)	[12]
			$ZnIn_2S_4$	420 nm cutoff filter	CO		40.4		[13]
			$ZnIn_2S_4$/N-doped graphene	300 W Xe lamp	CO	23.1	2.45		[14]
			porous carbon microtubule @In_2O_3 /$ZnIn_2S_4$	300 W Xe lamp	CO		101.62		[15]
			$Fe_2O_3@$ $ZnIn_2S_4$	Xe lamp	CO		37.13		[16]
TEA	CH_3CN		$ZnIn_2S_4$-$ZnAlO_x$	9 W 455 nm LEDs light	CO	60	1100		[17]
			$ZnIn_2S_4$	AM 1.5G	CO		276.7		[18]
		none	$ZnIn_2S_4$-Ni	300W Xe lamp	CO	5.5	138.3		[19]
			UCNPs/ZIS	300W Xe lamp	CO	60.7	52.84		[20]
			$ZnIn_2S_4$-In_2O_3	400 nm cutoff filter	CO	80	3075		[21]
			g-C_3N_4/Au /$ZnIn_2S_4$	300 W Xe lamp	CO	94.1	242.3		[22]
			CdS QDs/ $ZnIn_2S_4$	420 nm cutoff filter	CO	86.3	3340	1.36(420 nm)	[23]
TEOA			$ZnIn_2S_4/g$-C_3N_4	420 nm cutoff filter	CO	62.7	1453		[24]
	CH_3CN		O-doped $ZnIn_2S_4$	420 nm cutoff filter	CO		1680		[25]
		$Co(bpy)_3^{2+}$	$ZnIn_2S_4$@CNO	400 nm cutoff filter	CO	83.2	253.8		[26]
			$ZnIn_2S_4/g$-C_3N_4	Visible light	CO	87.8	892	2.4(420 nm)	[27]
			$CdIn_2S_4/ZnIn_2S_4$	400 nm cutoff filter	CO	71.5	1194.5		[28]
			$TiO_x/ZnIn_2S_4$	400 nm cutoff filter	CO		1095		[29]
			$L_{0.25}T_{0.75}$-ZIS	**420 nm cutoff filter**	**CO**	**97.9**	**5630**	**2.29 (420 nm)**	**This work**

The photocatalytic performance of $L_{0.25}T_{0.75}$-ZIS in this work was compared with ever reported $ZnIn_2S_4$ catalysts, and this work displayed at a fairly good level.

Table S5. Time-resolved PL decay lifetime

Photocatalysts	**τ_1(ns)** **A_1(%)**	**τ_2(ns)** **A_2(%)**	**Ave.τ(ns)**
L-ZIS	0.53 57.85	76.27 42.15	0.91
$L_{0.75}T_{0.25}$-ZIS	0.62 42.77	151.57 57.23	1.44
$L_{0.5}T_{0.5}$-ZIS	0.59 40.29	148.79 59.71	1.45
$L_{0.25}T_{0.75}$-ZIS	0.76 36.97	158.93 63.03	2.03
T-ZIS	0.63 36.96	156.94 63.04	1.70

The average emission lifetime of $L_{0.25}T_{0.75}$-ZIS (2.03 ns) was longer than that of other samples, which means that the separation efficiency of photogenerated charge carriers increased significantly due to the appropriate V_{Zn} of $L_{0.25}T_{0.75}$-ZIS.

Table S6. Fitting resistance of EIS

Photocatalysts	**R(Ohm)**
L-ZIS	77760000000000
$L_{0.75}T_{0.25}$-ZIS	31150
$L_{0.5}T_{0.5}$-ZIS	27250
$L_{0.25}T_{0.75}$-ZIS	14960
T-ZIS	19690

The improved transport of charge carriers of the $L_{0.25}T_{0.75}$-ZIS photocatalyst was further reflected in the lowest electric resistance as confirmed by the electrochemical impedance spectra (Figure 4d), in which the composite material manifested the smallest hemicycle radius. At the same time, we also gave the equivalent circuit diagram and fitting resistance value in the appendix to further prove this point. This observation demonstrated that the $L_{0.25}T_{0.75}$-ZIS photocatalyst could enhance the generation, separation, and transport of photoinduced charges, thus rendering high efficiency of CO_2 photoreduction.

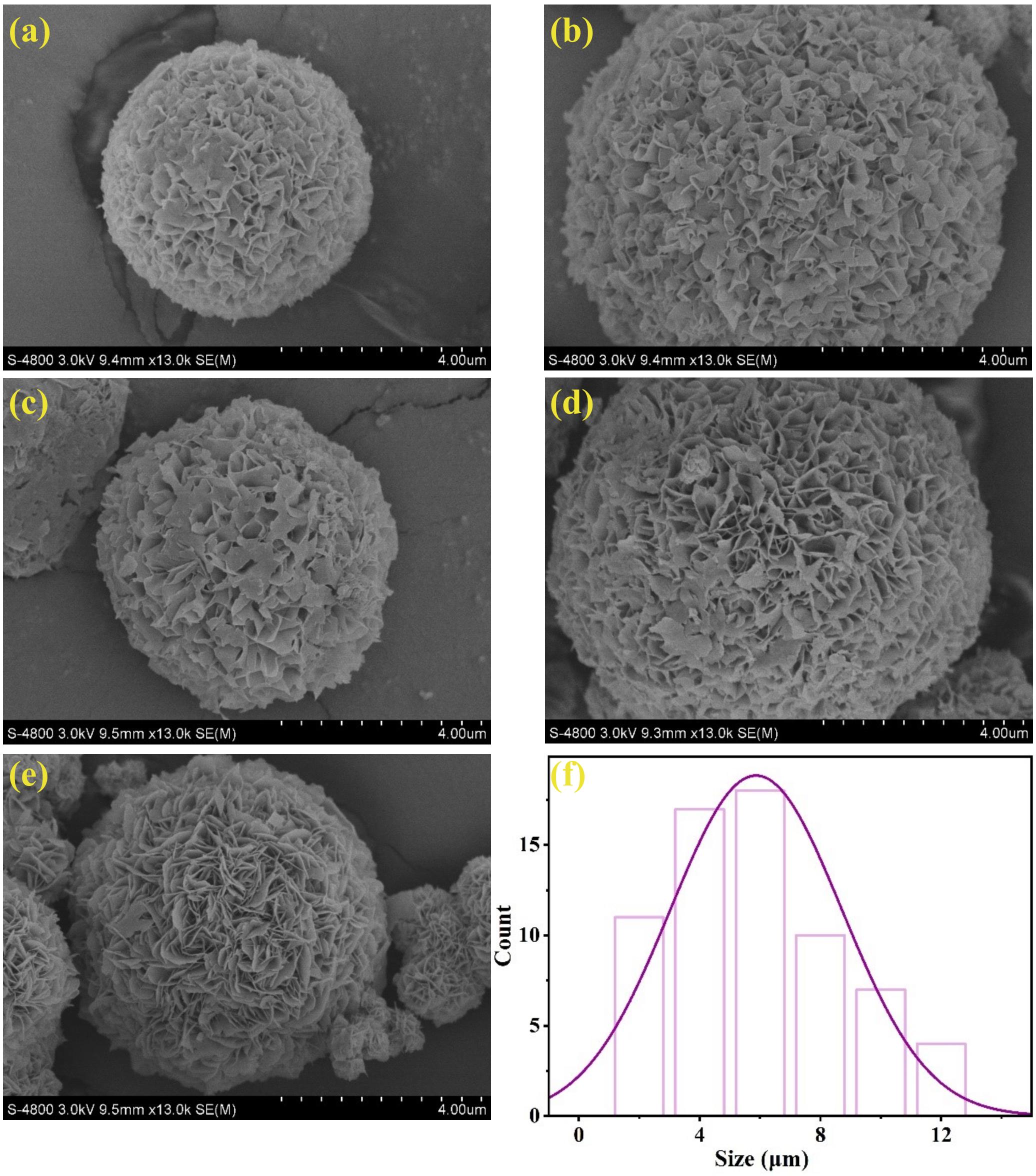

Figure S1. SEM of (a)L-ZIS; (b) L$_{0.75}$T$_{0.25}$-ZIS; (c) L$_{0.5}$T$_{0.5}$-ZIS; (d) L$_{0.25}$T$_{0.75}$-ZIS and (e) T-ZIS; (f) size distribution of L$_{0.25}$T$_{0.75}$-ZIS.

All samples presented 3D flower-like hierarchical structure-assembled nanosheet. With increase of Zn vacancies, nanosheet elicited lamellar irregularity and partly adhesion of edge, improved specific surface area. L$_{0.25}$T$_{0.75}$-ZIS presented 3D flower-like hierarchical structure-assembled nanosheet of 5.87 μm in diameter (**Figure S1f**).

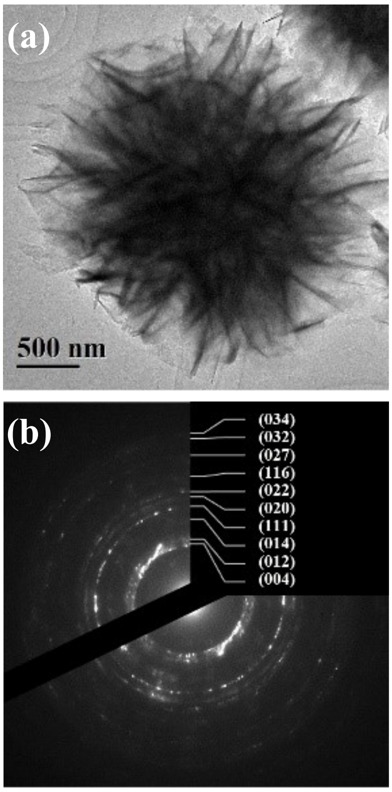

Figure S2. (a)TEM and (b) corresponding SAED pattern of $L_{0.25}T_{0.75}$-ZIS.

The selected area electron diffraction (SAED) image showed three bright rings indexed to (004), (012) and (111). Other different radii in the diffraction ring represent various $ZnIn_2S_4$ crystal planes, proved $ZnIn_2S_4$ synthesis successfully.

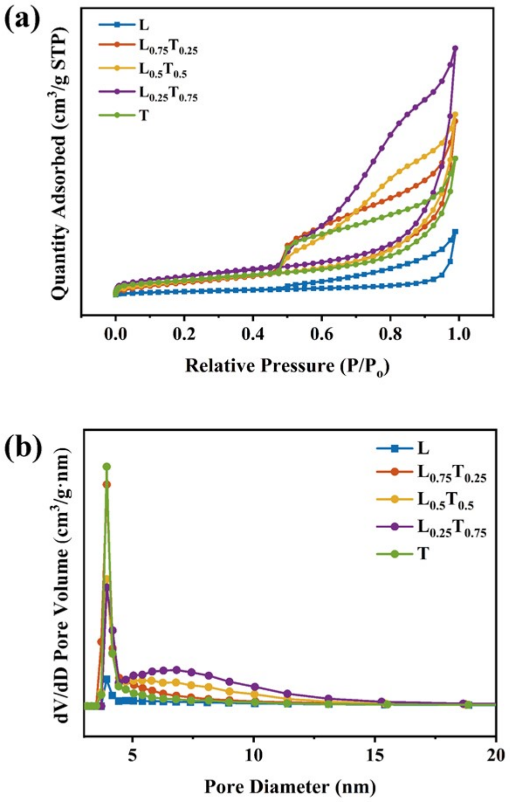

Figure S3. (a)Nitrogen adsorption-desorption isotherms and (b)pore-size distributions of L-ZIS, $L_{0.75}T_{0.25}$-ZIS, $L_{0.5}T_{0.5}$-ZIS, $L_{0.25}T_{0.75}$-ZIS and T-ZIS.

Expatiate on the result, type IV adsorption isotherm was shown in pressure range of 0.45-1.0 with a typical H3 hysteresis loop (according to Brunauer-Deming- Deming- Teller classification), indicating that the agglomeration of nanosheets resulted in the formation of crevice pore.

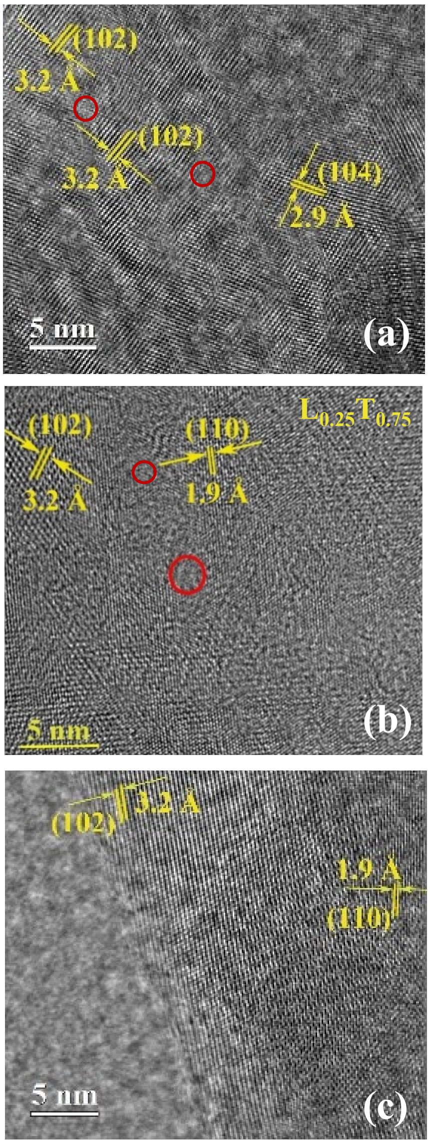

Figure S4. HR-TEM of (a)L-ZIS, (b)$L_{0.25}T_{0.75}$-ZIS and (d)T-ZIS.

L-ZIS had more V_{Zn} than $L_{0.25}T_{0.75}$-ZIS as red circle as S7 shown.

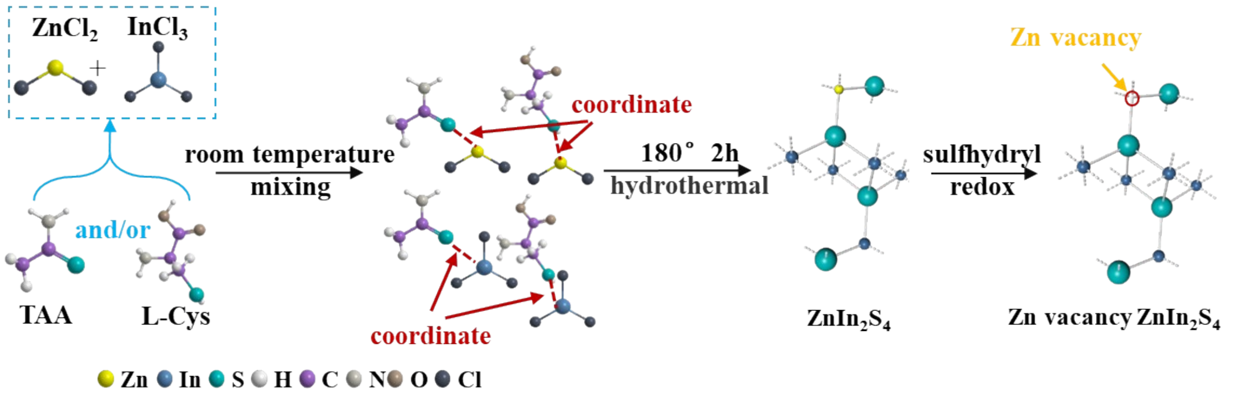

Figure S5. Scheme of sulfhydryl coordination regulated Zn vacancy-$ZnIn_2S_4$ synthesis process

Solution coordination model (SCM) was a favorable explanation to regulate $ZnIn_2S_4$ crystal structure which was reported previously,[30, 31] however, it cannot explain Zn vacancy formation. Herein, we upgraded this SCM process with a feasible synthesis route and illustrated the possible formation mechanism of Zn vacancy in $ZnIn_2S_4$ (**Figure S5**). The tetrahedral $[Zn\text{-}(TAA)_4]^{2+}$, $[Zn\text{-}(L\text{-}Cys)_4]^{2+}$, $[In\text{-}(TAA)_4]^{3+}$, $[In\text{-}(L\text{-}Cys)_4]^{3+}$ and octahedral $[In\text{-}(TAA)_6]^{3+}$, $[In\text{-}(L\text{-}Cys)_6]^{3+}$ were formed in reaction solution due to the coordinated function between Zn^{2+}/In^{3+} with TAA and/or L-Cys. As a result, $Zn\text{-}S_4$, $In\text{-}S_4$ and $In\text{-}S_6$ species were formed under hydrothermal condition, thereinto, Zn^{2+} possessed stronger interaction with the ligand due to smaller electronegativity relative to that of In^{3+}, which was one of the causes for Zn vacancy formation. Meanwhile, the strong reducibility of mercapto group in L-Cys, which was also confirmed by the not obvious weight loss peak but evident endothermic reaction at 29 ºC in TGA analysis (**Figure S6**), could partially reduce Zn^{2+} to Zn resulting in the formation of Zn vacancy.[32, 33] This TGA weight decline was ascribed to H loss due to the unstable mercapto group in L-Cys, meant L-Cys was easily possessing reducibility. Thus, various sulfhydryl groups were selected as comparable precursor to fabricate $ZnIn_2S_4$ with different Zn vacancy concentrations here.

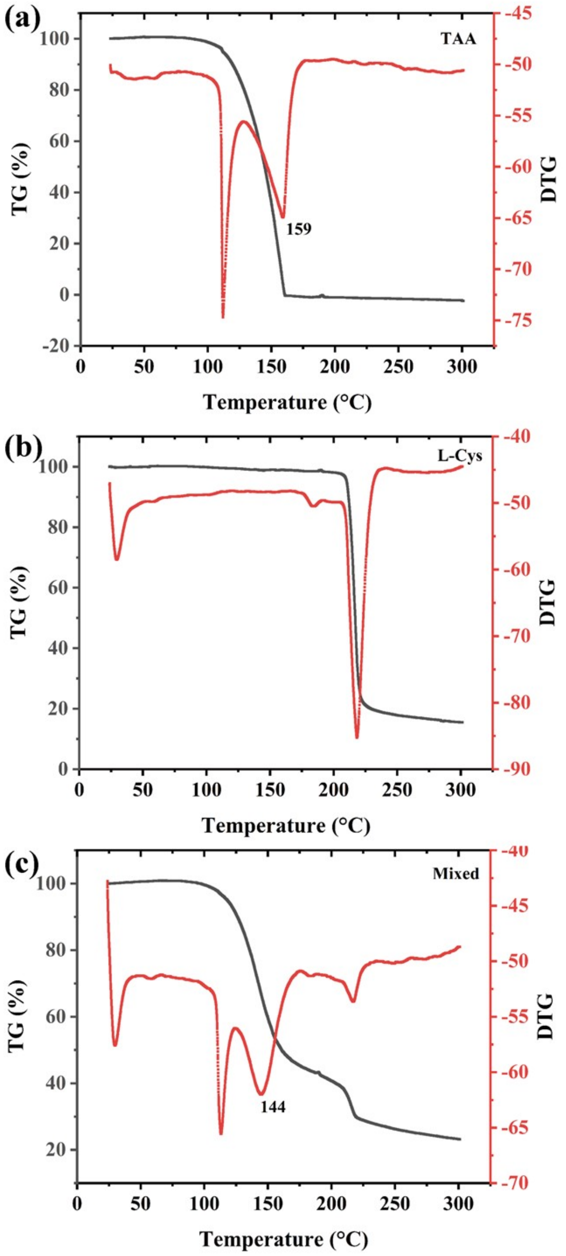

Figure S6. TGA of (a) TAA; (b) L-Cys and (c) mixed of TAA and L-Cys.

TGA of TAA, L-Cys and mixed TAA with L-Cys was analyzed at heating rate of 5 ^{o}C/min from room temperate to 300 ^{o}C in air. TGA of L-Cys showed a peak at 29 ^{o}C indexed to -SH loss H, and the peak didn’t move after introduced TAA. Meantime easy to loss H of L-Cys proved -SH had a strong reducibility.

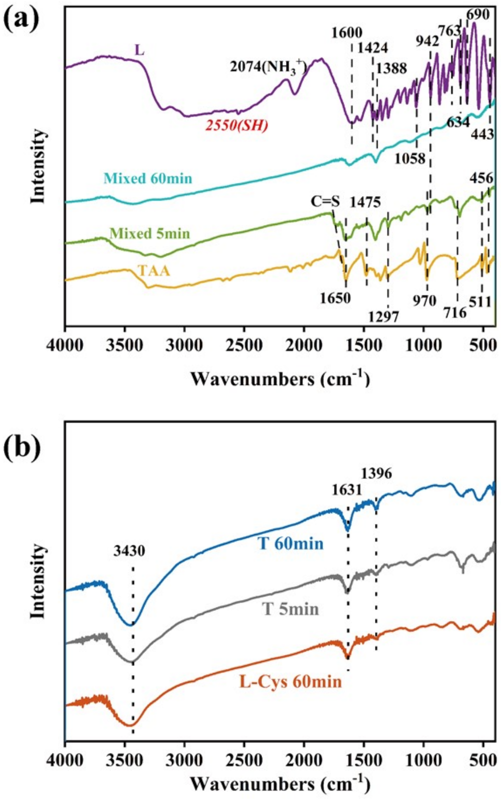

Figure S7. (a) FT-IR of TAA, L-Cys and fetched samples of $L_{0.25}T_{0.75}$-ZIS in the synthesis process, (b) FT-IR of fetched samples of T-ZIS and L-ZIS in the synthesis process.

FT-IR was used here to illustrate the formation mechanism of the coordination by Zn^{2+} or In^{3+} with TAA and/or L-Cys on $ZnIn_2S_4$ crystal structure and Zn vacancy formation. To analyze the reaction process more objectively, we fetched samples at 5 mins and 60 mins during hydrothermal reaction process (**Figure S7**). 5 mins' sample with TAA and L-Cys mixed was detected in FT-IR spectra, C=S bond was shifted from 1694 cm^{-1} to 1735 cm^{-1} ascribed to Zn^{2+}/In^{3+} combined with C=S formed M (metal)···S=C. Along with the hydrothermal reaction proceeded, the above-mentioned signal peak disappeared at 60 mins connoted that C=S was cracked and proved final synthetic sample had only M···S. The disappearance of -SH stretching mode at 2550 cm^{-1} supported the weight loss of H in L-Cys (which also proved by TGA analysis) formed M···S likewise. Dissimilarly, there was a slightly different performance on pure TAA sample, C=S in 5mins' sample was not detected due to the faster hydrolyze speed of TAA than that of L-Cys, which was ascribed to L-Cys could slowed down reaction speed greatly.[34] Logically, the coordination of TAA with Zn^{2+} or In^{3+} to form M···S=C resulted in without vacancies formation in $ZnIn_2S_4$. However, strong reducibility of L-Cys could lead to excessive Zn vacancy formation, which being carrier recombination center. It was necessary to control Zn vacancy concentrations via ligand environment regulation, and it was experimentally proved here that L-Cys could produce Zn vacancy while TAA was able to suppress this process precisely. Thus, by adjusting the amount of TAA and L-Cys addition, we realized an appropriate Zn vacancy concentration in $ZnIn_2S_4$ to achieve the desired CO_2 photoreduction performance ($L_{0.25}T_{0.75}$-ZIS).

FT-IR of fetched samples of pure TAA and pure L-Cys at different synthesis times were showed above. C=S in 5mins' sample was not detected due to the faster hydrolyze speed of TAA than that of L-Cys, which was ascribed that L-Cys could slowed down reaction speed greatly. Nine species in FT-IR for TAA or L-Cys were detected. The peak at 2074 cm^{-1} was confirmed as the specie of NH_3^+.[35] The peak at 1600 cm^{-1} was assigned to the bond of N-H in NH_3 asymmetry bending vibration and 763 cm^{-1} was its rocking vibration. The peak at 634 cm^{-1} was indexed to N-H signal. CCO vibration was observed at 1424 cm^{-1} and the stretching symmetry frequency of OCO group in sample was found at 1388 cm^{-1}, COH was matched with the peak at 1058 cm^{-1}. These NH_3 peaks and C species were disappeared after hydrothermal process for 60 mins. 942 cm^{-1} was coincided with SH bending vibration. 690 cm^{-1} was corresponding to γCS stretching vibration. 443 cm^{-1} was accorded with CCN bending vibration [36]. These peaks demonstrated our L-Cys was pure. 1650 cm^{-1} in yellow line was NH_2 bending region and 1297 cm^{-1} was agreed with its rocking bend. 970 cm^{-1} was concurred with CC stretching (ʋCC) vibrational mode. 716 cm^{-1} was fitted with CS bond (ʋCS) and 511 cm^{-1} was squared to γCS. 456 cm^{-1} was consistent in NCS bending mode (βNCS) [37]. Above peaks showed TAA was not contaminated.

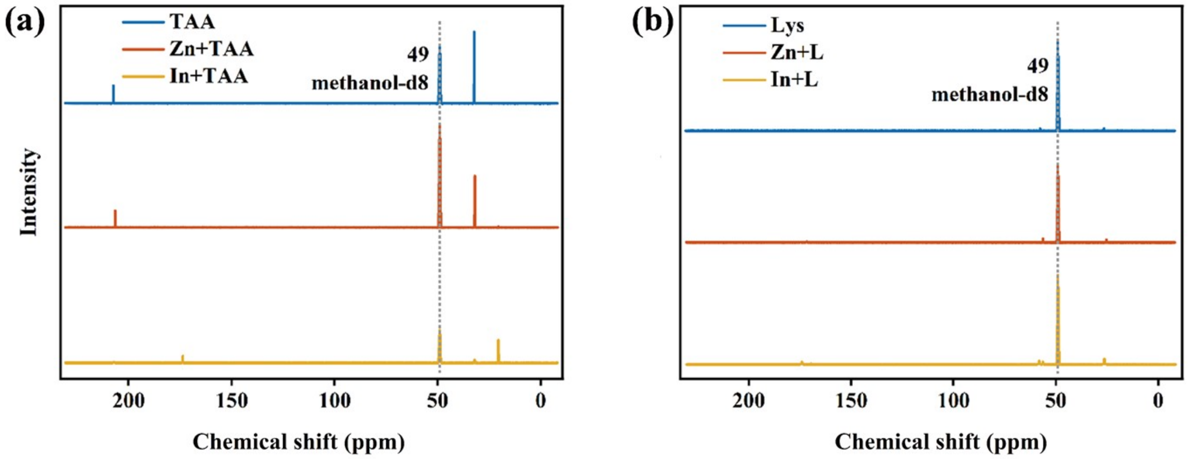

Figure S8. ^{13}C NMR of (c) TAA and (d) L-Cys with Zn^{2+}/In^{3+}

^{13}C NMR data was displayed above after they were remediated with methanol-d8 at the position of 49 ppm. In order to distinguish other peaks more clearly, different forms of expression were used in the main text.

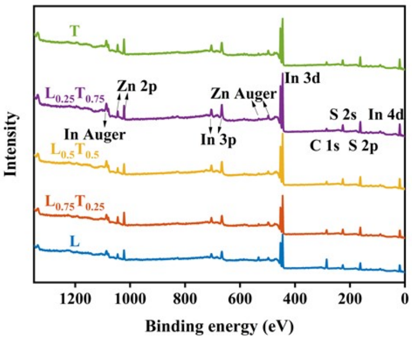

Figure S9. (a) Full spectrum X-ray photoelectron spectroscopy spectra

The full spectrum showed the presence of the characteristic lines of the constituent elements Zn, In and S in the samples. A significant peak at 284.8 eV could be indicated as amorphous carbon species from atmospheric CO_2 or XPS instruments.

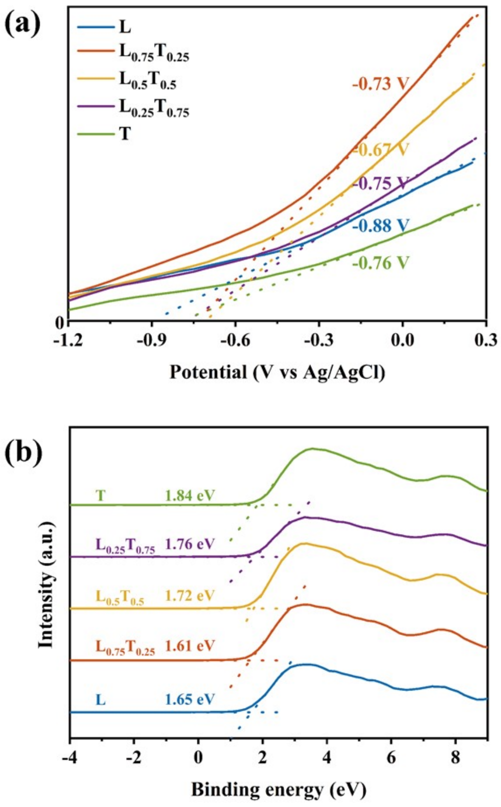

Figure S10. (a) Mott-Schottky and (b) XPS-valence band of L-ZIS, $L_{0.75}T_{0.25}$-ZIS, $L_{0.5}T_{0.5}$-ZIS, $L_{0.25}T_{0.75}$-ZIS and T-ZIS.

All the linear plots possessed positive slopes, indicating that the V_{Zn} didn't change $ZnIn_2S_4$ semiconductor type. These samples all belonged to n-type semiconductors. The flat band potential was from -0.67 to -0.88 V (vs. Ag/AgCl, pH=7), calculated by standard potentials of reference electrodes (the equations $E_{Ag/AgCl}$ =E_{RHE}-0.0591pH-0.197 and E_{NHE} = E_{RHE}-0.0591pH) the flat band potential results was -0.473 to -0.683 (vs NHE, pH=7). And gap between conductive band and flat band is 0.1-0.2 for n-type semiconductors, $ZnIn_2S_4$ exactly is n-type direct band gap semiconductor. It is approximated that the flat band potential tested when Ag/AgCl as reference electrode is approximately equal to conduction band of materials. Since the reduction potentials of CO_2/CO and H_2O/H_2 are -0.52 and -0.41 V (vs NHE, pH=7) nevertheless. All of catalysts was thermodynamics feasible for CO_2 reduction.

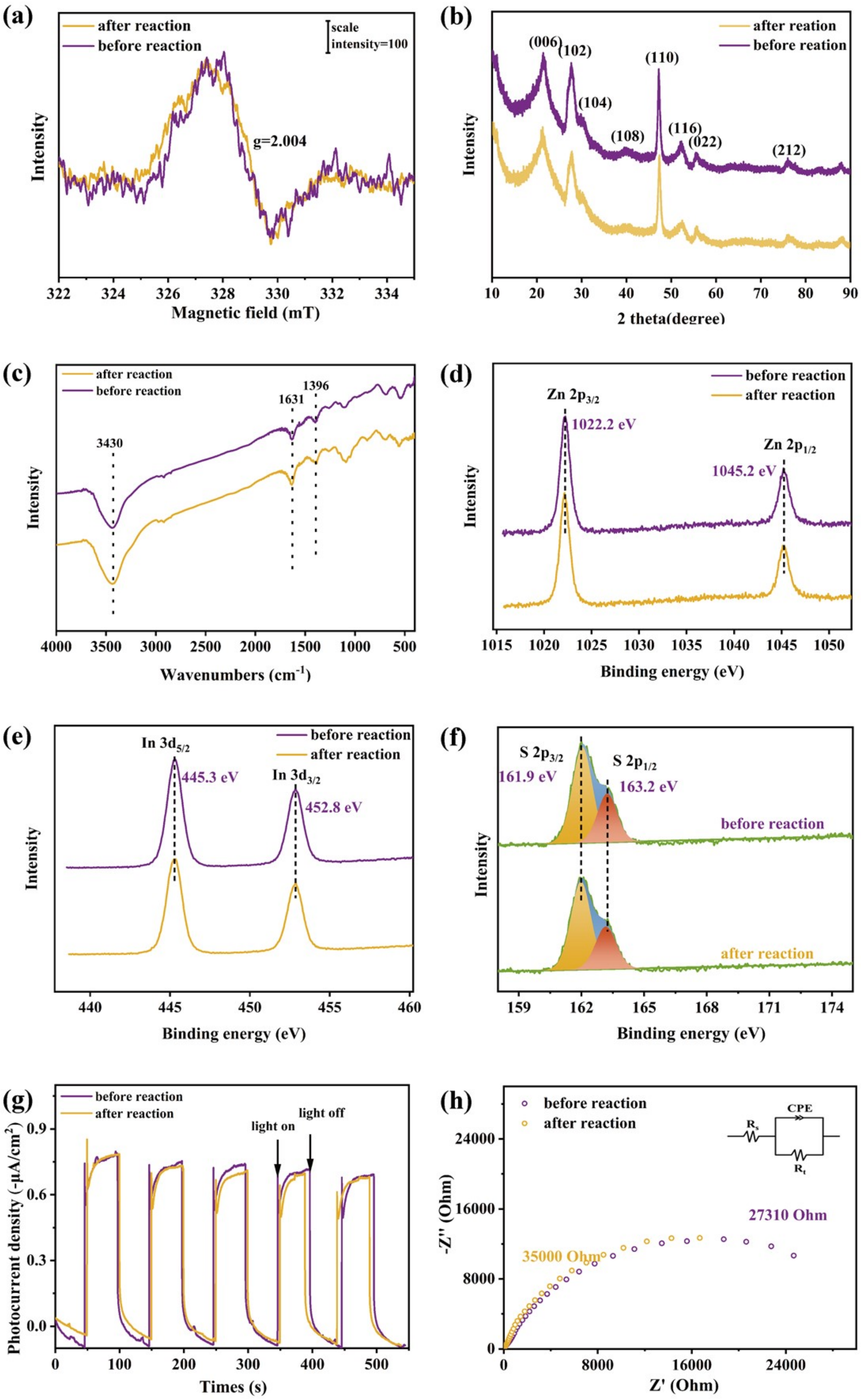

Figure S11. (a) EPR; (b) XRD; (c) FT-IR pattern; (d-f) high resolution XPS (g) Photo response current and (h) electrochemical impedance spectroscopy of $L_{0.25}T_{0.75}$-ZIS before and after photocatalytic CO_2 reduction process.

In spite of the fact that the photocatalytic reduction cycle performance of $L_{0.25}T_{0.75}$-ZIS exhibited a well stable property, it is necessary to expound the corresponding reason from the angle of crystal structure, chemical state and photochemical property. We compared and analyzed materials achieved before and after photocatalytic reduction using EPR, XRD, FT-IR, XPS and photochemical characterize. We proved the fabricated V_{Zn} concentrations were necessary to achieve our excellent performance, therefore, the stability of V_{Zn} concentrations was demonstrated using ESR and revealed a confirmed stability (Figure S11). No obvious structure variation of $L_{0.25}T_{0.75}$-ZIS was detected by XRD demonstrated photocatalytic reduction process did not influence the stability of $ZnIn_2S_4$ crystal. Logically, it is quite prominent for heterogeneous catalysis that the final product was or not desorbed effectively from the surface of photocatalyst, which ensured valid formation of desired resulted products and reusability. No CO was scanned on our photocatalyst after reaction from FT-IR spectra guaranteed process. Sulfide metal catalyst was usually unstable came from S^{2-} instability, binding energy of S^{2-} did not change after reaction demonstrated synthesized $ZnIn_2S_4$ was satisfactorily durable. Photo response current and EIS demonstrated electron migration was also stable. In a word, no obviously change in V_{Zn} concentrations, crystal structure, surface function groups, chemical state and electrochemical property testified $L_{0.25}T_{0.75}$-ZIS had a good stability.

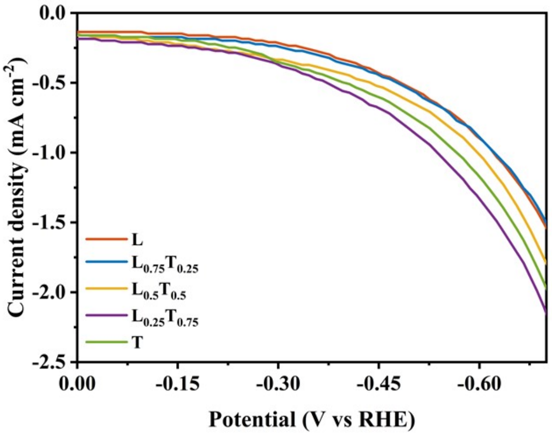

Figure S12. Linear sweep voltammetry of L-ZIS, $L_{0.25}T_{0.75}$-ZIS, $L_{0.5}T_{0.5}$-ZIS, $L_{0.75}T_{0.25}$-ZIS and T-ZIS.

The linear sweep voltammetry (LSV) curves confirmed the most accelerated interfacial charge separation and migration over $L_{0.25}T_{0.75}$-ZIS again.

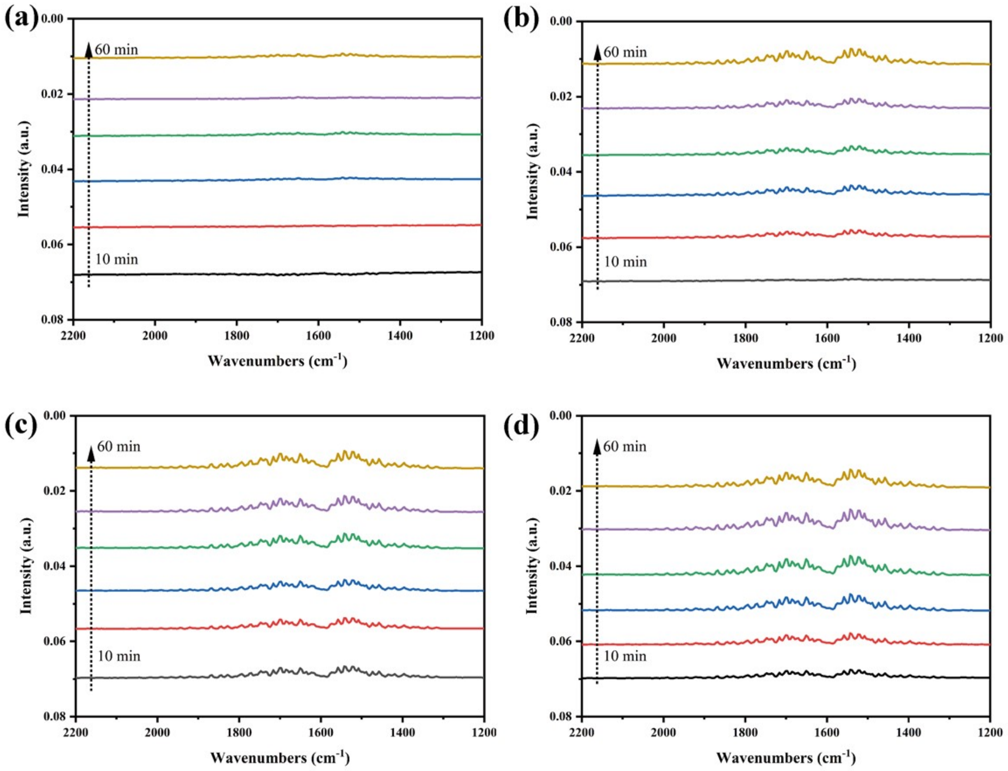

Figure S13. (a) in-situ FT-IR spectra for co-adsorption of a mixture of CO_2 and H_2O on (a)L-ZIS, (b) $L_{0.25}T_{0.75}$-ZIS, (c) $L_{0.5}T_{0.5}$-ZIS and (d) T-ZIS

Upon light irradiation, the peak became intensitive (Figure. S12). Under same condition, the peak intensity in activation behaviors followed the sequence that $L_{0.25}T_{0.75}$-ZIS＞T-ZIS＞$L_{0.5}T_{0.5}$-ZIS＞$L_{0.75}T_{0.25}$-ZIS＞L-ZIS.

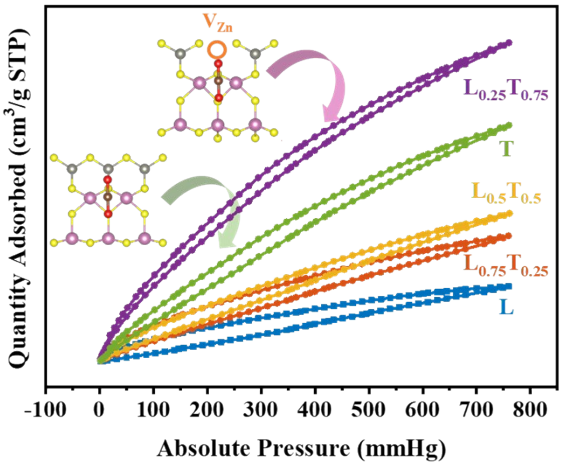

Figure S14. CO_2 adsorption and desorption of L-ZIS, $L_{0.25}T_{0.75}$-ZIS, $L_{0.5}T_{0.5}$-ZIS, $L_{0.75}T_{0.25}$-ZIS and T-ZIS

$L_{0.25}T_{0.75}$-ZIS had strongest CO_2 adsorption capacity than the other samples.

Reference:

1. G. Kresse and J. Furthmüller, *Phys. Rev. B*, 1996, **54**, 11169-11186.
2. G. Kresse, *J. Non-Cryst. Solids*, 1995, **192-193**, 222-229.
3. S. Grimme, *J. Comput. Chem.*, 2006, **27**, 1787-1799.
4. S. Grimme, *J. Comput. Chem.*, 2004, **25**, 1463-1473.
5. J. K. Nørskov, J. Rossmeisl, A. Logadottir, L. Lindqvist, J. R. Kitchin, T. Bligaard and H. Jónsson, *J. Phys. Chem. B*, 2004, **108**, 17886-17892.
6. A. A. Peterson, F. Abild-Pedersen, F. Studt, J. Rossmeisl and J. K. Nørskov, *Energ. Environ. Sci.*, 2010, **3**, 1311-1315.
7. Y. Zhao, Y. Chen, L. Du, Q. Wang, X. Liu, L. Li and G. Tian, *J. Colloid Interface Sci.*, 2022, **605**, 253-262.
8. D. Jiang, Q. Zhang, D. Chen, B. Wen, Q. Song, C. Zhou and D. Li, *J. Alloys Compd.*, 2021, **865**, 158836.
9. G. Yang, D. Chen, H. Ding, J. Feng, J. Zhang, Y. Zhu, S. Hamid and D. W. Bahnemann, *Appl. Catal. B Environ.*, 2017, **219**, 611-618.
10. Y. Ding, Y. Chen, Z. Guan, Y. Zhao, J. Lin, Y. Jiao and G. Tian, *ACS Appl. Mater. Interfaces.*, 2022, **14**, 7888-7899.
11. Q. Han, L. Li, W. Gao, Y. Shen, L. Wang, Y. Zhang, X. Wang, Q. Shen, Y. Xiong, Y. Zhou and Z. Zou, *ACS Applied Materials & Interfaces*, 2021, **13**, 15092-15100.
12. X. Jiao, Z. Chen, X. Li, Y. Sun, S. Gao, W. Yan, C. Wang, Q. Zhang, Y. Lin, Y. Luo and Y. Xie, *J. Am. Chem. Soc.*, 2017, **139**, 7586-7594.
13. Y. Wu, H. Wang, W. Tu, S. Wu and J. W. Chew, *Appl. Catal. B Environ.*, 2019, **256**, 117810.
14. Y. Xia, B. Cheng, J. Fan, J. Yu and G. Liu, *Sci. China Mater.*, 2020, **63**, 552-565.
15. W. Gao, L. Wang, C. Gao, J. Liu, Y. Yang, L. Yang, Q. Shen, C. Wu, Y. Zhou and Z. Zou, *Nanoscale*, 2020, **12**, 14676-14681.
16. Z. Zhao, C. Shi, Q. Shen, W. Li, D. Men, B. Xu, Y. Sun and C. Li, *CrystEngComm*, 2020, **22**, 8221-8227.
17. Y. Shao, X. Wang, Z. Dou, X. Liang, X. Zhang, M. Pang, Q. Xu, M. Ji and M. Wang, *Catal. Sci. Technol.*, 2021, **11**, 3422-3427.
18. Y. He, H. Rao, K. Song, J. Li, Y. Yu, Y. Lou, C. Li, Y. Han, Z. Shi and S. Feng, *Adv. Funct. Mater.*, 2019, **29**, 1905153.
19. J. Wang, Y. M. Xuan and K. Zhang, *Catal. Sci. Technol.*, 2021, **11**, 4012-4015.
20. M. Yu, X. Lv, A. Mahmoud Idris, S. Li, J. Lin, H. Lin, J. Wang and Z. Li, *J. Colloid Interface Sci.*, 2022, **612**, 782-791.
21. S. Wang, B. Guan and X. Lou, *J. Am. Chem. Soc.*, 2018, **140**, 5037-5040.
22. G. Zhang, X. Zhu, D. Chen, N. Li, Q. Xu, H. Li, J. He, H. Xu and J. Lu, *Environ. Sci. Nano*, 2020, **7**, 676-687.
23. Z. Zhu, X. Li, Y. Qu, F. Zhou, Z. Wang, W. Wang, C. Zhao, H. Wang, L. Li, Y. Yao, Q. Zhang and Y. Wu, *Nano. Res.*, 2020, **14**, 81-90.
24. B. Khan, F. Raziq, M. B. Faheem, M. U. Farooq, S. Hussain, F. Ali, A. Ullah, A. Mavlonov, Y. Zhao, Z. R. Liu, H. Tian, H. H. Shen, X. T. Zu, S. Li, H. Y. Xiao, X. Xiang and L. Qiao, *J. Hazard. Mater.*, 2020, **381**, 120972.
25. B. Pan, Y. Wu, B. Rhimi, J. Qin, Y. Huang, M. Yuan and C. Wang, *J. Energy Chem.*, 2021, **57**, 1-9.
26. K. Zhu, O. Y. Jie, Q. Zeng, S. G. Meng, W. Teng, Y. H. Song, S. Tang and Y. J. Cui, *Chinese J. Catal.*, 2020, **41**, 454-463.
27. M. Zhou, S. Wang, P. Yang, Z. Luo, R. Yuan, A. M. Asiri, M. Wakeel and X. Wang, *Chem. Eur. J.*, 2018, **24**, 18529-18534.
28. G. Zhang, Z. Wang, T. He, J. Wu, J. Zhang and J. Wu, *Chem. Eng. J.*, 2022, **442**, 136309.
29. H. Shi, J. Du, H. Wang, Z. Jia, D. Jin, J. Cao, J. Hou and X. Guo, *Chem. Eng. J.*, 2022, **440**, 135735.
30. X. Gou, F. Cheng, Y. Shi, L. Zhang, S. Peng, J. Chen and P. Shen, *J. Am. Chem. Soc.*, 2006, **128**, 7222-7229.
31. M. A. Sriram, P. H. Mcmichael, A. Waghray and P. N. Kumte, *J. Mater. Sci.*, 1998, **33**, 4333-4339.
32. C. Siva, C. N. Iswarya, P. Baraneedharan and M. Sivakumar, *Mater. Lett.*, 2014, **134**, 56-59.
33. B. Bai, M. Xu, N. Li, W. Chen, J. Liu, J. Liu, H. Rong, D. Fenske and J. Zhang, *Angew. Chem. Int. Ed.*, 2019, **58**, 4852-4857.
34. W. Pudkon, S. Kaowphong, S. Pattisson, P. J. Miedziak, H. Bahruji, T. E. Davies, D. J. Morgan and G. J. Hutchings, *Catal. Sci. Technol.*, 2019, **9**, 5698-5711.
35. B. Koleva, M. Spiteller and T. Kolev, *Amino Acids*, 2010, **38**, 295-304.
36. A. Pawlukojc, J. Leciejewicz, A. J. Ramirez-Cuesta and J. Nowicka-Scheibe, *Spectrochim. Acta A Mol. Biomol. Spectrosc.*, 2005, **61**, 2474-2481.
37. S. Góbi, I. Reva, G. Tarczay and R. Fausto, *J. Mol. Struct.*, 2020, **1220**, 128719.